



HAL
open science

A computational fluid dynamic study of the filling of a gaseous hydrogen tank under two contrasted scenarios

Rémi Gonin, Pierre Horgue, Romain Guibert, David Fabre, Rémi Bourguet,
Fouad Ammouri, Elena Vyazmina

► **To cite this version:**

Rémi Gonin, Pierre Horgue, Romain Guibert, David Fabre, Rémi Bourguet, et al.. A computational fluid dynamic study of the filling of a gaseous hydrogen tank under two contrasted scenarios. International Journal of Hydrogen Energy, 2022, 47 (55), pp.23278 - 23292. 10.1016/j.ijhydene.2022.03.260 . hal-03720305

HAL Id: hal-03720305

<https://hal.science/hal-03720305v1>

Submitted on 18 Jul 2022

HAL is a multi-disciplinary open access archive for the deposit and dissemination of scientific research documents, whether they are published or not. The documents may come from teaching and research institutions in France or abroad, or from public or private research centers.

L'archive ouverte pluridisciplinaire **HAL**, est destinée au dépôt et à la diffusion de documents scientifiques de niveau recherche, publiés ou non, émanant des établissements d'enseignement et de recherche français ou étrangers, des laboratoires publics ou privés.

A computational fluid dynamic study of the filling of a gaseous hydrogen tank under two contrasted scenarios

Rémi GONIN^{a,b,*}, Pierre HORGUE^a, Romain GUIBERT^a, David FABRE^a,
Rémi BOURGUET^a, Fouad AMMOURI^b, Elena VYAZMINA^b

^a*Institut de mécanique des fluides de Toulouse (IMFT), Université de Toulouse, CNRS, 2
allée Camille Soula, Toulouse, France*

^b*Air Liquide Innovation Campus Paris, 1 Chemin de la Porte des Loges, Les
Loges-en-Josas, France*

Abstract

The filling of a horizontal hydrogen tank designed for light duty vehicles is investigated by means of multi-physics numerical simulations. The simulation approach, implemented in OpenFOAM, includes compressible Reynolds-Averaged Navier-Stokes (RANS) modeling of the fluid flow and heat transfer in the solid parts. The simulations are carried out for 2D-axisymmetric and 3D configurations. Two filling scenarios of the tank, leading to two distinct thermal behaviors, i.e. homogeneous versus heterogeneous, are simulated and compared to the experimental data issued from the HyTransfer project. In the homogeneous case, where no thermal stratification occurs, the 2D and 3D simulation results are close to the experimental ones. A phenomenon of jet flapping is identified via the 3D simulation. In the heterogeneous case, where thermal stratification occurs, the 3D simulation captures an averaged temperature close to the experimental one, as well as the instant at which the thermal gradients appear. It also captures the deflection of the jet, which is a central element in the emergence of the thermal gradients.

Keywords: compressed hydrogen, tank filling, thermal gradient, CFD
2010 MSC: 00-01, 99-00

Highlights

- 2D axisymmetric and 3D simulations are carried out using free software OpenFOAM.
- Jet deflection and flapping, and onset of stratification are captured.

*Corresponding author

Email address: `remi.gonin@toulouse-inp.fr` (Rémi GONIN)

- The $k - \omega$ SST turbulence model underestimates the thermal gradients.

1. Introduction

10 1.1. Context

Hydrogen is currently considered as an alternative source of energy for light and heavy vehicles compared to regular fossil fuel [1]. For practical convenience, the filling time of the hydrogen tank of light duty vehicle should be comparable to that of a standard fuel tank, about 3-5 minutes [2], for a similar operation range, i.e. 500 km. To match these requirements, the internal pressure reaches 15 70 MPa at a standard temperature. Composite and plastic materials are employed in order to limit tank weight. These materials are characterized by much lower thermal conductivities [3] compared to metallic tanks, leading to reduced heat exchanges with the exterior environment and to a sharp rise of the gas and wall temperatures. The J2601 standard of the Society of Automobile Engineers 20 (SAE) organism [4] advises admissible temperature between $-40\text{ }^{\circ}\text{C}$ and $85\text{ }^{\circ}\text{C}$. Inner temperatures need to be controlled following these specifications.

As shown in previous studies [5, 6, 7], reducing the inlet temperature is a possible way to decrease the maximum temperature reached during the filling. 25 As a result, current filling stations precool the inlet flow down to $-40\text{ }^{\circ}\text{C}$ to reduce the final gas temperature in the tank. However, this solution presents some limitations. It is energetically costly and, considering that the temperature field may be heterogeneous during filling due to buoyancy effects, high temperatures may be reached along the upper walls even with precooling. This heterogeneous thermal field phenomenon has been highlighted during the HyTransfer project 30 [8], funded by the Fuel Cells and Hydrogen Joint Undertaking (FCH JU) partnership. This program involved experiments and computational fluid dynamics (CFD) in two institutions, Air Liquide Advanced Technology (ALAT) and the Joint Research Centre (JRC). With thermal sensors located inside the hydrogen bulk, the thermal behavior of the fluid has been investigated and showed internal thermal gradients for some tank geometries and under some specific filling 35 conditions. However, the limited number of probes within the fluid region did not allow to clarify the mechanism leading to thermal gradients.

Historically, the first attempts to model tank filling were based on thermodynamic zero dimension (0D) models, which consider the fluid bulk as a unique 40 control volume on which mass and energy balance equations are applied (see e.g [9, 10, 11, 12]). These models are suitable to obtain rapid estimations of the averaged temperature of the inner fluid. When reducing the injection velocity, thermal gradients appear in the tank and 0D models cannot capture local temperature variations. Terada et al. [13] observed that this transition occurs 45 below a critical injection velocity of 5 m/s . This criterion was confirmed on HyTransfer cases [14] and gives insights into the occurrence of thermal gradients; however the underlying physical phenomena still need to be explored.

With the increase of computer resources, CFD can now be employed to investigate these configurations. CFD gives access to the entire velocity, pressure 50

and temperature fields, which are inaccessible via experiments. The HyTransfer experimental database has served as a benchmark for validation of the simulations in both involved teams. On one hand, within JRC team, simulations were carried out with the commercial CFD software Ansys CFX, using a Redlich-Kwong [15] equation of state as real gas equation of hydrogen. For turbulence modeling, in the first study belonging to the HyTransfer project [16], a modified $k - \epsilon$ turbulence model [17] previously used in similar studies from the same team [5, 18, 19, 20] was used. Subsequently, in Refs. [21, 22] a $k - \omega$ shear stress transport (SST) model with a $\Gamma - \Theta$ model transitional turbulent-laminar model described by Langtry et Menter [23] was used to improve the capture of heterogeneities. These simulations captured the onset of thermal stratification but tended to be less reliable to quantify the stratification level. On the other hand, in the ALAT team, simulations were done with the commercial CFD software Ansys Fluent Inc. using a half domain composed of 640 000 cells, a $k - \omega$ SST turbulence model and real gas model data tabulated from REFPROP© v9.1 database. These simulations were able to predict the onset of stratification phenomenon but not the gradient values.

1.2. Case selection from experimental data

To avoid exceeding the temperature limit of 85 °C during the filling, the injected gas is cooled which is energetically costly. The HyTransfer project [8] aimed at optimizing fast filling of compressed hydrogen tank using an experimental setup, to find new filling protocols, limiting the pre-cooling, while guaranteeing safety. In this project, three tanks have been used: (i) a type III tank, i.e. composite material with metal liner, capacity of 40 L, provided by Dynetek Industries Ltd, (ii) a type IV tank, i.e. composite material with plastic liner, capacity of 37 L, and (iii) a type IV tank capacity of 531 L provided by Hexagon. The first two are considered as small tanks with an aspect ratio L/D (tank length over tank inner diameter) about 2.7 and 2.4. The aspect ratio of the third one is about 5.5. All tanks have been placed in horizontal position, the gravity is normal to the tank axis. The main filling parameters are the inlet mass flowrate and the injection diameter.

The present study will only focus on small tanks for light vehicles. Given the reported cases which lead to different results in terms of thermal gradients, the Hexagon 37 L appears to be the best candidate to run CFD validation. For each experimental case, the local temperature has been recorded at selected points. There are 10 probes for ALAT and 6 for JRC. Consequently, local information about the thermal field is limited by the number and location of the probes. To compare the different results, a quantification of the thermal gradients is needed. Based on the available data [24], the maximum difference between the highest probe temperature T_{max} and the averaged probe temperature T_{av} is proposed as an indicator of heterogeneity at each time. Table 1 presents ALAT results. Results from JRC [25] showed the same trend.

For the present study, the best case and the worst case scenarios have been selected: (i) a case with quasi uniform thermal field for 3 mm injection diameter and 8 g/s averaged mass flowrate, which will be named the **homogeneous** case,

	ⓇHexagon 37 L					
Injection diameter [mm]	3	3	6	6	10	10
Averaged mass flowrate [g/s]	2	8	2	8	2	8
Injection velocity* [m/s]	[190;4.2]	[280;17]	[62;1.1]	[73;2.0]	[22;0.41]	[28;1.1]
ALAT: $T_{max} - T_{av}$ [°C]	8.36	6.35	26.76	11.28	30.03	24.39

Table 1: Thermal gradients for the 37 L ⓇHexagon tank from ALAT[24]. Selected cases in bold. *Estimated assuming a uniform velocity profile in the pipe and using the density calculated via the measured inlet temperature and pressure in the tank, the measured mass flowrate and pipe cross section.

and (ii) a case with large thermal gradient for 10 mm injection diameter and 2 g/s averaged mass flowrate, which will be named the **heterogeneous** case. Note that for the heterogeneous case, the 10 mm injection diameter corresponds to filling directly into the plug aperture without an injection pipe, while for the homogeneous case, an injection pipe of 3 mm of diameter and 100 mm length is entering into the hydrogen bulk. As more probes are available, the ALAT experimental data were chosen for the present calculations. The experimental absolute pressure in the bulk and local temperatures will be used to set the initial and boundary conditions and to validate the numerical method.

1.3. Objectives of this work

The main objective of the present study is to capture, numerically, the different thermal behaviors which occur during tank filling. The different injection scenarios involve physical phenomena related to the three-dimensional nature of the problem so three-dimensional (3D) simulations are carried out. Particular attention is paid to the 3D nature of the underlying physical phenomena and to the impact of a 2D-axisymmetric assumption on their prediction. A specificity of the present study is the use of the open-source software OpenFOAM [26]. (version 6.0 from CFD Direct Ltd).

2. Physical system and its modeling

2.1. Physical system

During gas injection in a closed volume, the pressure and temperature gradually rise. Figure 1 represents the physical configuration. The tank is laying along its main axis, the x-axis, in a horizontal position and the incoming gas is injected along the x-direction. The gravity (\mathbf{g}) is acting vertically along the y-axis. The tank is axisymmetric around the x-axis. It is composed of 4 or 5 solid regions, depending on the presence of an injection pipe: (i) a composite wrap which undergoes the mechanical constraint due to gas pressure, (ii) a plastic liner which limits the molecular diffusion of hydrogen through the wall, (iii) metallic bosses and (iv) plugs at each tank extremities and (v) a metallic injection pipe (for the homogeneous case). The fluid region is the volume enclosed by the solid regions. The tank is surrounded by air at atmospheric pressure and temperature.

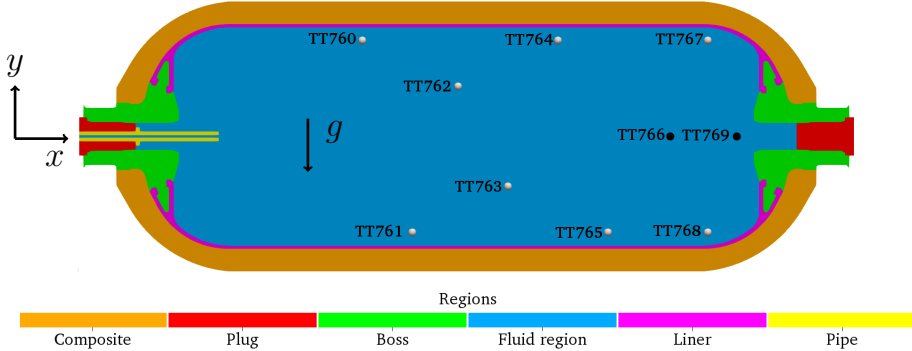


Figure 1: Hexagon 37 *L* tank with a 3 mm injection cut through the (x,y) plane. Probe locations are indicated by circles: probes located in the (x,y) plane in white and probes located outside the (x,y) plane in black.

The simulations are initialized using the pressure and temperature values from the issued experiments. The temperature data come from 10 probes located in the fluid region. Probe locations are given in the HyTransfer project document [24] and shown in figure 1. The inlet temperature and tank pressure were also measured and reported in [24]. Figure 2, adapted from [24], shows plots of all probe measurement for the homogeneous case (plot A) and heterogeneous case (plot B). The results emphasize the contrasted thermal behaviors between the two cases: (i) in the homogeneous case, all probe temperatures remain close to each other for each part; (ii) for the heterogeneous case, the temperatures diverge at $t \approx 100$ s .

2.2. Model

The simulation is based on a coupled fluid dynamics and heat transfer model, called conjugate heat transfer (CHT) [27] method. Depending if the region is fluid or solid, different sets of models and equations are considered.

In solid regions, the governing equation is the energy conservation equation, in order to calculate temperature diffusion across walls. As experiments have been carried out outdoors without control of the environmental conditions, the temperature was not uniform at the beginning of the filling. Assuming a negligible impact of the initial temperature disparity on the final fluid and liner temperatures, all tank regions were initialized at the averaged temperature of the fluid region. Thermophysical properties are constant and can be found in table 2.

On the boundaries, a perfect thermal contact is assumed between the different solid regions, continuity of the heat flux and temperature on walls in contact between solid regions. Heat transfers between the outer faces and the atmosphere are modeled by Newton law,

$$q = hS\Delta T , \quad (1)$$

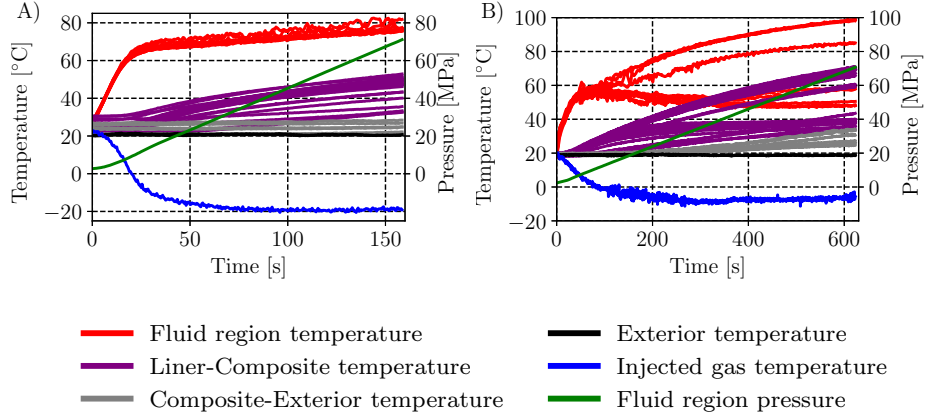


Figure 2: Experimental values from hyTransfer [24]: A) the homogeneous case, B) the heterogeneous case.

Region	Material	Thermal conductivity [W/m/K]	Specific heat capacity [J/kg/K]	Density [kg/m ³]
Composite	Carbon Fiber	0.616	783	1365
Liner	Polymer	0.414	1799	914
Boss	Aluminium 6061	167	896	2700
Plug	Stainless Steel 316L*	16.2	120	7990
Pipe	Stainless Steel 316L*	16.2	120	7990

Table 2: Thermophysical properties of the solid regions. *An erroneous value was used for the specific heat capacity of the stainless steel 316L, which should be close to 500 [J/kg/K]. The plug and the pipe represent a marginal fraction of the solid tank mass and the impact of this error is therefore negligible.

150 with q [W] the thermal flux, h [W/m²/K] the heat transfer coefficient, S [m²] the surface, and ΔT [K] the difference between the solid temperature and the exterior temperature. As set in the JRC work [16, 18, 20], $h = 6$ W/m²/K and the external temperature is set to 18 °C, based on the experimental data values.

155 In the fluid region, the governing equations are the Navier-Stokes equations, i.e. the mass, momentum and energy conservation equation. The Reynolds number based on the pipe diameter, injection velocity and viscosity ranges from 15 000 to 45 000 for the heterogeneous case and from 50 000 to 600 000 for the homogeneous case. At these Reynolds numbers, the flow is turbulent [28] at the pipe outlet. The turbulence is modeled using the Boussinesq assumption with
160 an unsteady Reynolds-averaged Navier–Stokes (URANS) approach and the $k-\omega$ SST equations [29]. This model was shown to be accurate in a fully developed turbulent region like a jet flow [30, 31] and in a pipe flow [32, 33]. Assuming that Prandtl number is close to 1, i.e. the thermal boundary layer and the velocity boundary layer have similar thicknesses, it is expected to capture the
165 thin thermal layer, with an adequate mesh.

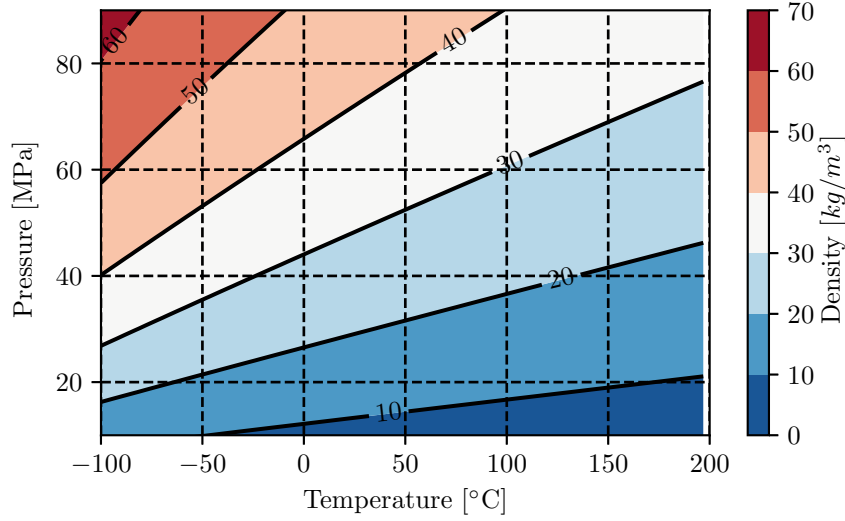


Figure 3: Hydrogen density as a function of pressure and temperature, issued from NIST [37].

Concerning the boundary conditions, for the turbulent kinetic energy k and the turbulent dissipation rate ω , no wall law is used in the heterogeneous case and a wall law (in OpenFOAM, `kLowReWallFunction`) [34] is employed in the homogeneous case. A no slip condition is used on the walls for the velocity. At the inlet, a uniform mass flowrate is imposed. It is deduced from the experimental pressure input as represented in figure 2 (green curve). For the temperature, a continuity of temperature and heat flux is imposed between the different regions. As the perfect gas approximation is not valid in the considered range of pressure and temperature, real gas data are required to determine the thermodynamical properties. In the literature, several gas models have been used and details can be found in the review [35] and [36]. Here, the relevant properties of hydrogen are obtained using the National Institute of Standards and Technology (NIST) tabulated data from [37]: (i) the density [kg/m^3], (ii) the thermal conductivity [$W/m/K$], (iii) the specific thermal capacity [$J/kg/K$], (iv) the kinematic viscosity [$kg/m/s$] and (v) the specific enthalpy [J/kg]. These properties are read from tables. For example, figure 3 represents a plot of the density table as a function of pressure and temperature.

3. Numerical Method

3.1. Solver


The most suitable solver in OpenFOAM is called `chtMultiRegionFoam` [38] as it is required, in the fluid region, to simulate a transient, buoyant and turbulent flow, which exchanges heat with walls. The `ChtMultiRegionFoam` solver

can run a transient simulation with two algorithms. The Pressure Implicit with
190 Splitting of Operators (PISO) algorithm [39, 40], solves the coupled momen-
tum and density equations. The thermodynamic properties (such as density,
viscosity, conductivity) are computed explicitly using the last known pressure
and temperature values. It involves one velocity predictor step and, by default,
two pressure corrector steps at each temporal iteration, to calculate the velocity
195 and pressure fields. To maintain the stability and accuracy of the simulation, it
is recommended to use a Courant–Friedrichs–Lewy number (CFL), lower than
1.

The PIMPLE algorithm [41] is named after a contraction of the PISO and the
Semi-Implicit Method for Pressure Linked Equations (SIMPLE) [42] algorithms.
200 It consists in executing, at each time step, several PISO iterations with updated
thermodynamic properties of the fluid, using the last known solution. With
this iterative process, $CFL > 1$ is allowed, i.e. larger time steps and faster
computations.

No significant difference has been observed in the results by using these
205 two algorithms. The decision of using one instead of the other was motivated
by the possible reduction in computation time. The PIMPLE algorithm was
used for the homogeneous case and the PISO algorithm for the heterogeneous
case. Regarding time and space discretization, first order schemes were used
to maintain the stability of the simulations. Both cases ran using constrained
210 maximum CFL values, with time step ranging from 10^{-4} s to 10^{-6} s .

3.2. Mesh

The meshing process is based on a 3D CAD model from Hexagon provided
during the HyTransfer project [8]. The mesh was generated with two open-
source tools: (i) Salome [43], and (ii) cfMesh [44]. Figure 4A shows a general
215 view of the 3D meshes in the (x,y) plane. Here, focus is placed on the meshing
strategy of the fluid region, which is more challenging than the solid regions.
The objective is to generate a mesh mainly composed of hexahedral cells, with
a refinement adapted to the expected physics. The difference of scales between
the inner pipe area and the main bulk require a variable refinement strategy to
220 reach the relevant cell size in each region. A view at the injection region can be
found in figure 4B. A typical cell size in the bulk is to 5mm. Considering that a
turbulent jet typically expands with an angle of 12° [45], the refinement follows
a conical shape, with a slightly larger angle. Figure 4C visualizes this region. In
the boundary layer regions, the mesh is composed of five layers with a growth
225 rate of 1.4. This design leads to $y^+ < 1$ on all walls for the heterogeneous case,
and a wall law is not required. For the homogeneous case, $y^+ \approx 1$ could not be
reached in the the injection region, a $y^+ < 50$ was enforced and a wall law is
used.

3D simulations have been carried out: (i) on the full tank geometry, or (ii)
230 on half of the domain using as a cutting plane (x,y). The first ones will be named
full 3D and the second ones **3D**. In addition to the 3D meshes, 2D axisymmetric
meshes, named **2D**, were also employed. These meshes represent a slice of the

Case	Type	Fluid region	Solid regions	Total
Homogeneous	2D	15 605	6 373	21 978
	3D	816 156	493 243	1 309 399
	full 3D	1 664 904	986 486	2 651 390
Heterogeneous	2D	11 273	5 873	17 146
	3D	651 482	449 126	1 100 608
	full 3D	1 302 964	898 252	2 201 216

Table 3: Number of cells for each case, in the fluid and solid regions.

domain with one cell depth. They have the same refinement property as the 3D meshes. The number of cells for each mesh is reported in table 3.

235 3.3. Validation

Validation of the solver and mesh was performed on the 2D cases in order to reduce computational costs. The homogeneous configuration was chosen for mesh convergence study, due to its higher velocities. Even though gravity is not taken into account in the 2D approach, the thermal gradients are limited in this configuration and the 2D results can be compared with the experimental data. Three cases were simulated, using a coarse mesh (9 193 cells), a medium mesh (15 605 cells) and a fine mesh (34 378 cells). Less than 1 °C of difference in the averaged temperature was noted over the integration time. The medium mesh was selected to design the 3D mesh. Time step sensitivity was studied on this medium mesh by dividing the time step by a factor of 2. This leads to less than 1 °C of difference in the averaged temperature.

245 Full 3D case and 3D case were compared over 15 seconds in the homogeneous case; the differences in temperature are negligible. In order to limit the computation cost, complete simulations were performed on the 3D cases, i.e. half of the tank. This strategy was also used by the JRC [16] and ALAT [46].

4. Results and discussion

4.1. Velocity and temperature fields

255 Figures 5, 6, 7, 8 show snapshots of the velocity magnitude (upper panel) and the temperature field (lower panel) at three different times over a filling scenario, for the 2D and 3D homogeneous cases, and the 2D and 3D heterogeneous cases. A x-axis symmetry is applied to the 2D cases to ease visualization. For the homogeneous case, the velocity colorbar is scaled between 0 and 10 *m/s* to highlight the jet penetration and the velocity decay over time. For heterogeneous case, the velocity colorbar is scaled between 0 and 1 *m/s*, for the same purpose.

260 Complementary videos of 3D cases are available in the **Supplemental Data**. For each case: the maximum magnitude of velocity is at the top left corner, an averaged value of the thermal field is indicated at the bottom left corner and an isoline of the averaged value of the thermal field is superimposed on the thermal field (bottom panel).

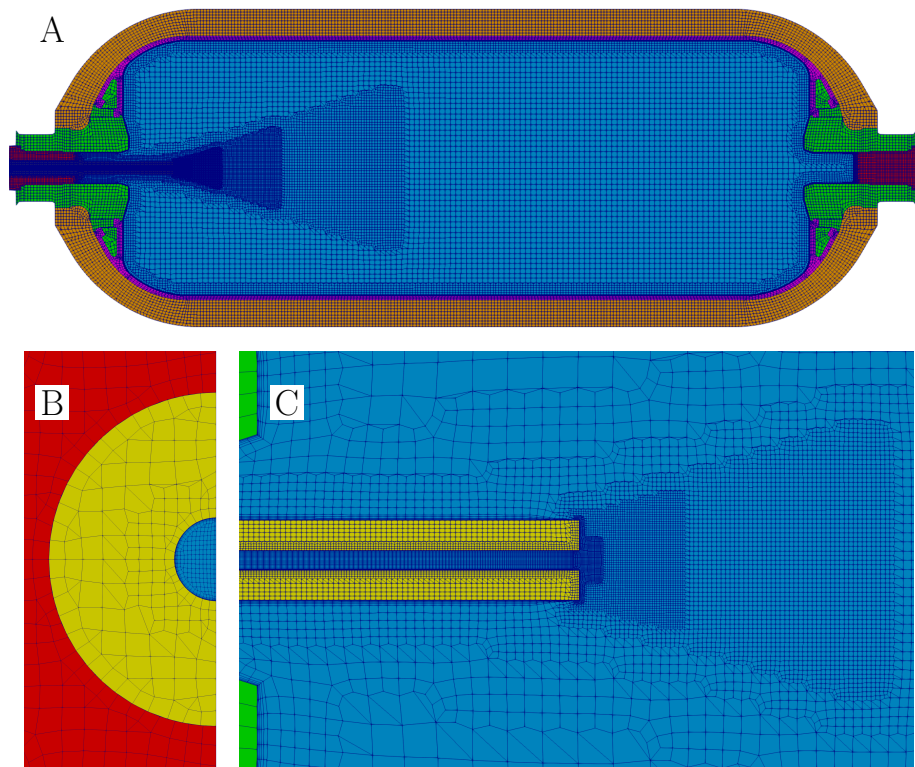


Figure 4: Computational meshes: A) a global overview of all regions in the (x,y) plane for the homogeneous case, B) slice at the inlet plane for the heterogeneous case, C) zoom around the injector for the heterogeneous case.

265 Supplementary video related to this article can be found at <https://doi.org/10.1016/j.ijhydene.2022.03.26>

In the 2D simulations (figures 5 and 7), due to the axisymmetry assumption, gravity is neglected. High temperature spots appear in the regions which are not reached by the cold jet, like the areas above and below the pipe, close to the liner and left boss wall. The jet remains parallel to the x-axis.

270 For the 3D homogeneous case (figure 6), the jet is flapping up and down in the (x,y) plane. In the video, it can be seen that the maximum temperature is not localized in the upper part but is oscillating around the injection area, with the same frequency as the jet flapping frequency. The thermal field is homogeneous, i.e. not vertically stratified.

275 For the 3D heterogeneous case (figure 8), before 50 s the jet is moving upward, as in the initial phase of flapping, but then it starts deflecting toward the lower part. A vertical gradient of temperatures appears, which is depicted by the horizontal isoline of temperature (lower panels at $t = 310$ s and $t = 610$ s in figure 8).

280 4.2. Global quantities

In the experiments, temperatures are sampled by a limited number of probes. An arithmetic average on probes may not be a representative value for an averaged temperature of the entire thermal field. Using the CFD, it is possible to average directly the temperature field

$$T_{av-field} = \frac{\sum_i T_i v_i}{V_{tank}}, \quad (2)$$

285 by weighting each cell temperature T_i by the cell volume v_i over the total volume V_{tank} , or to average the 10 temperature values $T_{probe,i}$ where probes are experimentally located

$$T_{av-probes} = \frac{\sum_i^{10} T_{probe,i}}{10}. \quad (3)$$

290 Due to its higher thermal disparity, the heterogeneous case is more relevant to compare over these two averaging approaches. The difference is lower than 1.5 °C before $t = 100$ s and lower than 0.5 °C after $t = 100$ s. Therefore, the averaged temperature from the experimental probes will be regarded as the reference value for further comparisons. The same question arises for the absolute pressure. CFD results show that the pressure field is close to uniform in the tank. Therefore, a single measurement point in the tank is already relevant
295 to characterize the bulk pressure.

Figure 9 presents a comparison of the averaged temperature and pressure between the 2D, 3D and experimental cases, for the homogeneous case A) and for the heterogeneous case B). Figure 10 presents the heat flux q (4) which can be calculated by

$$q = \sum_i \lambda_{eff} \Delta T s_i, \quad (4)$$

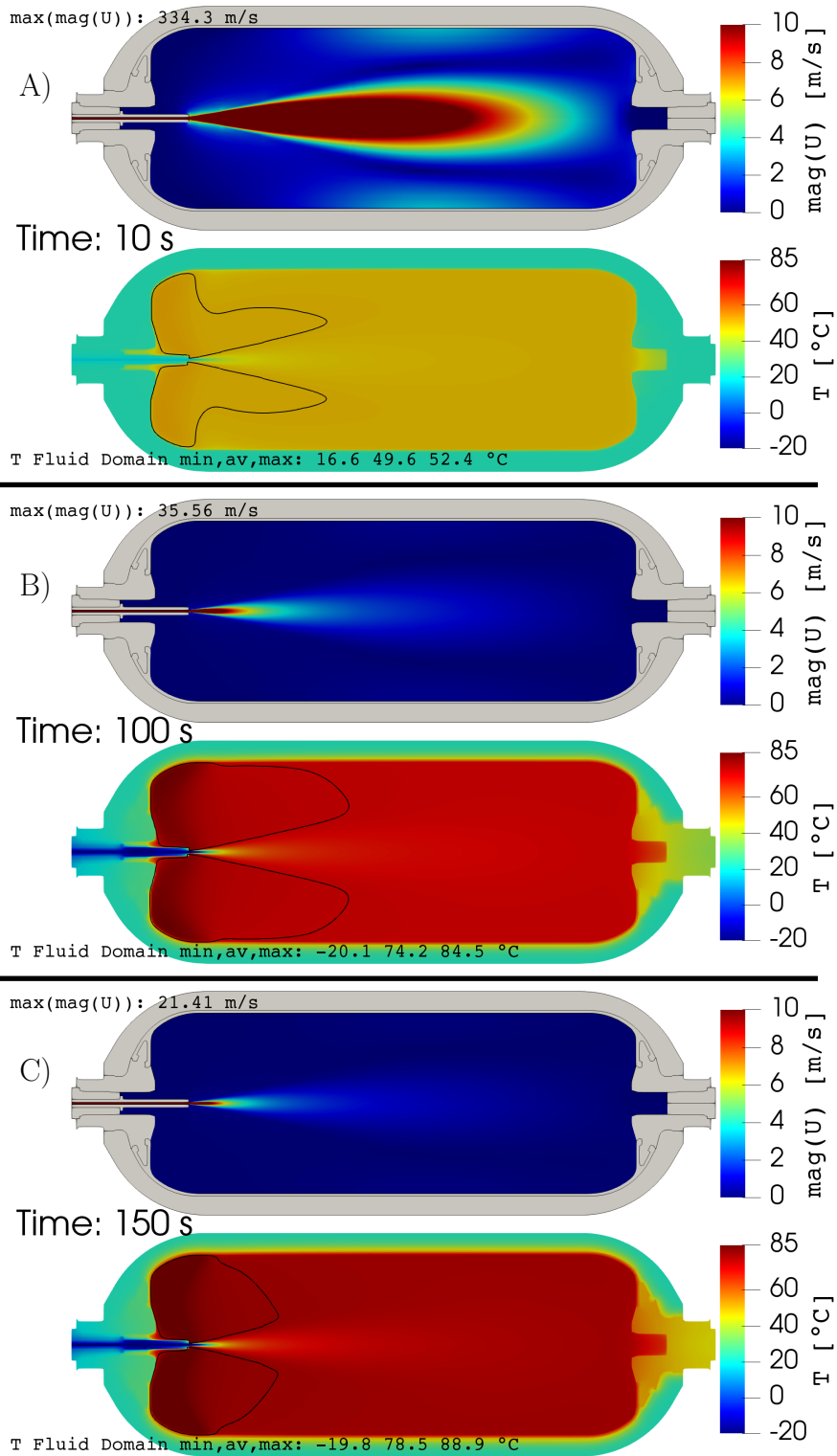


Figure 5: Homogeneous 2D case. For each time instant: A) $t = 10$ s, B) $t = 100$ s and C) $t = 150$ s. The upper panel represents the velocity magnitude field, the lower panel represents the temperature field. The black isoline corresponds to averaged temperature. A x-axis symmetry is applied to ease visualization.

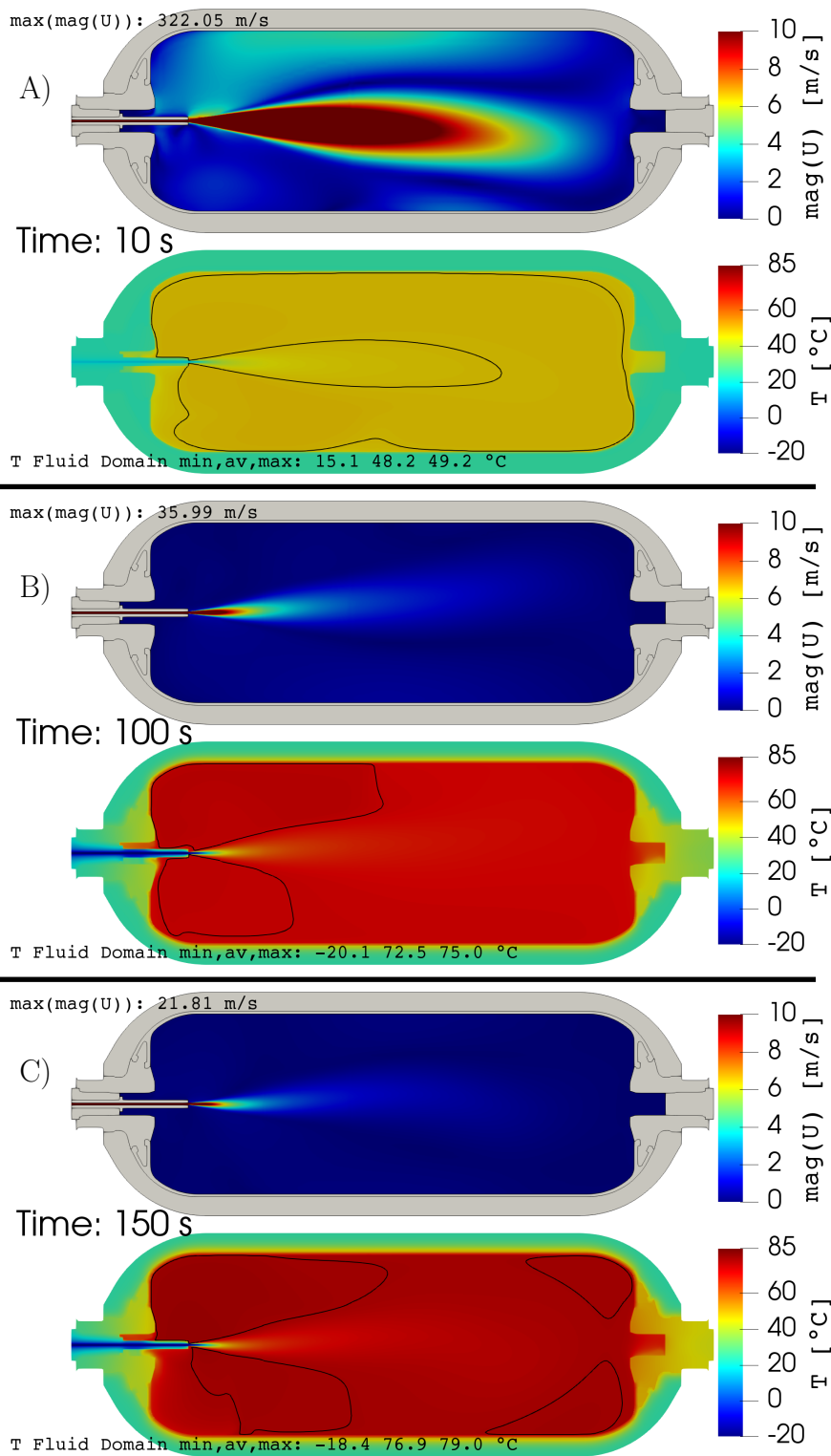


Figure 6: Homogeneous 3D case. For each time instant: A) $t = 10$ s, B) $t = 100$ s and C) $t = 150$ s. The upper panel represents the velocity magnitude field, the lower panel represents the temperature field. The black isoline corresponds to averaged temperature.

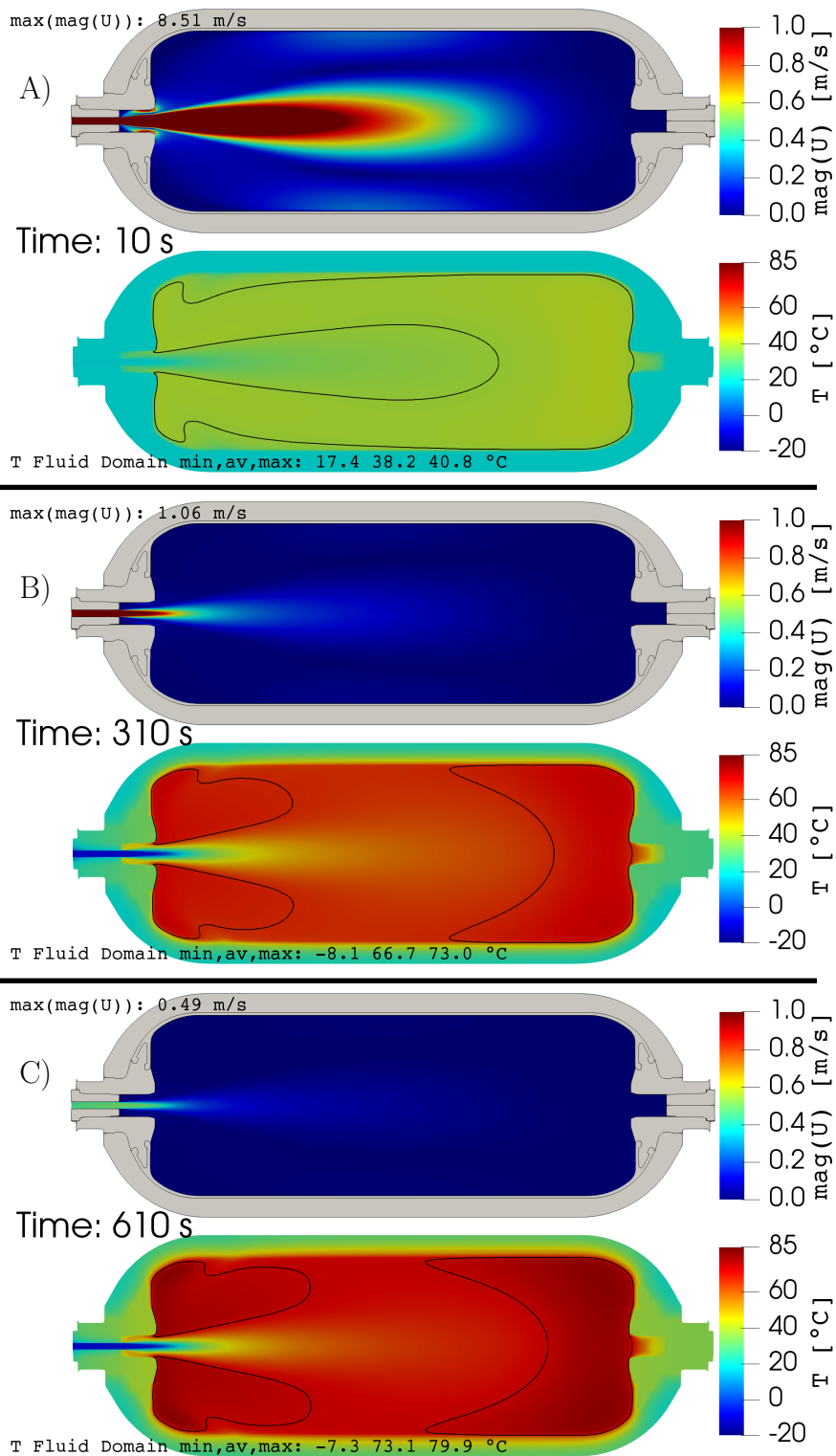


Figure 7: Heterogeneous 2D case. For each time instant: A) $t = 10$ s, B) $t = 310$ s and C) $t = 610$ s. The upper panel represents the velocity magnitude field, the lower panel represents the temperature field. The black isoline corresponds to averaged temperature. A x-axis symmetry is applied to ease visualization.

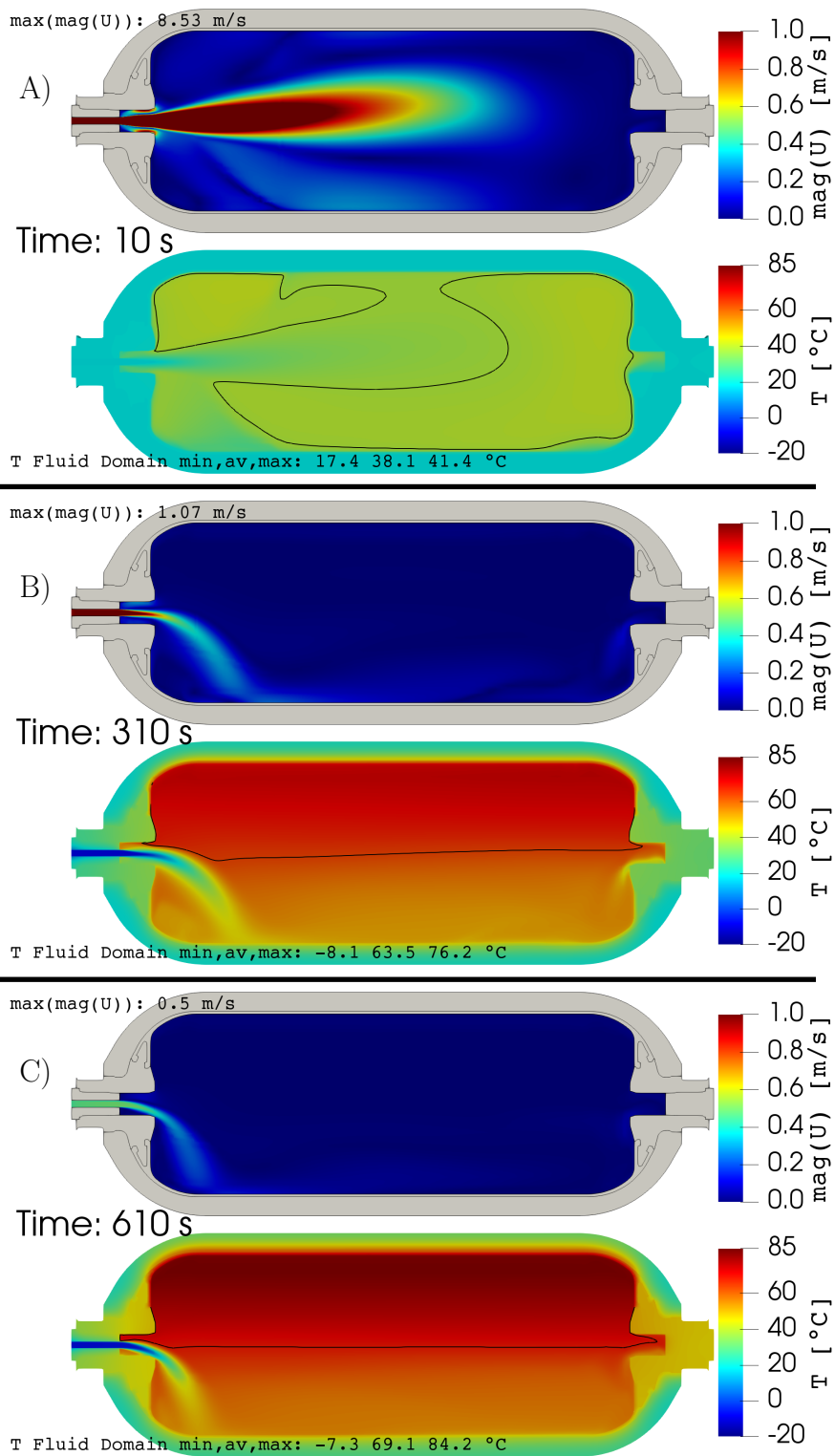


Figure 8: Heterogeneous 3D case. For each time instant: A) $t = 10$ s, B) $t = 310$ s and C) $t = 610$ s. The upper panel represents the velocity magnitude field, the lower panel represents the temperature field. The black isoline corresponds to averaged temperature.

where s_i is the cell surface at wall, ΔT is the difference of temperature between the one at wall and the one at the first cell center and λ_{eff} [W/m/K] is the effective thermal conductivity defined as

$$\lambda_{eff} = \lambda + \lambda_t , \quad (5)$$

where λ is the thermal conductivity and λ_t is the turbulent thermal conductivity,

$$\lambda_t = \frac{c_p \mu_t}{Pr_t} , \quad (6)$$

with the turbulent Prandtl number $Pr_t = 0.85$; c_p [J/kg/K] is the specific heat capacity and μ_t [kg/m/K] the turbulent dynamic viscosity.

Figure 10 displays the averaged surface temperature at fluid-solid interfaces using the following expression to weight the average using a local surface:

$$T_{wall} = \frac{\sum_i T_i s_i}{S} |_{fluid-solid\ wall} . \quad (7)$$

In the above expression, T_i is the cell temperature at wall, s_i is the cell surface at wall and S is the total surface of the wall.

Concerning the homogeneous case, figure 9A shows that the averaged temperature issued from the 3D field is within ± 1 °C from the experimental value. In the 2D case, the averaged temperature is higher and farther from the experimental value, compared to the 3D case. This difference of averaged temperature is induced by a difference of heat transfer. Figure 10A shows that the global heat flux (dotted line) is slightly larger for the 3D case than for the 2D case. This small difference is due to less heat flux through bosses and plugs for the 2D case. The larger flux through the liner does not counterbalance this trend. For the 2D case the gravity is neglected and therefore no natural convection is possible. In areas where heat transfer is led by natural convection, like plug cavity, the heat flux is underestimated. In addition, the 2D assumption constrains the jet on the x-axis, while it is free to flap in the (x,y) plane in the 3D case. This may result in a better mixing of the bulk and avoid some stagnant hot or cold spots. As shown in figure 10C, the deviations of heat flux is associated with large deviations in wall temperature predictions between the 2D and 3D simulations.

Concerning the heterogeneous case, the probe averaged temperature issued from the 3D simulations is within ± 3.5 °C from the experimental value before $t = 300$ s , and ± 1 °C after, as showing in figure 9B. The 2D case shows again a higher averaged temperature. In the heterogeneous case, gravity plays a role even more important than in the homogeneous case. As can be seen in figure 8, due to buoyancy forces, the jet tends to plunge towards the lower part of the tank. In the 2D axisymmetric case, this phenomenon and the vertical thermal stratification cannot be captured. This leads to a non physical thermal disparity and to an underestimation of the velocity close to the bottom wall (figure 7). A consequence is a significant difference of heat transfer on every walls, between the 2D and 3D cases, as highlighted in figure 10B. As shown in figure 10C, this leads to lower temperatures on solid walls, even though the averaged temperature in the fluid region is higher.

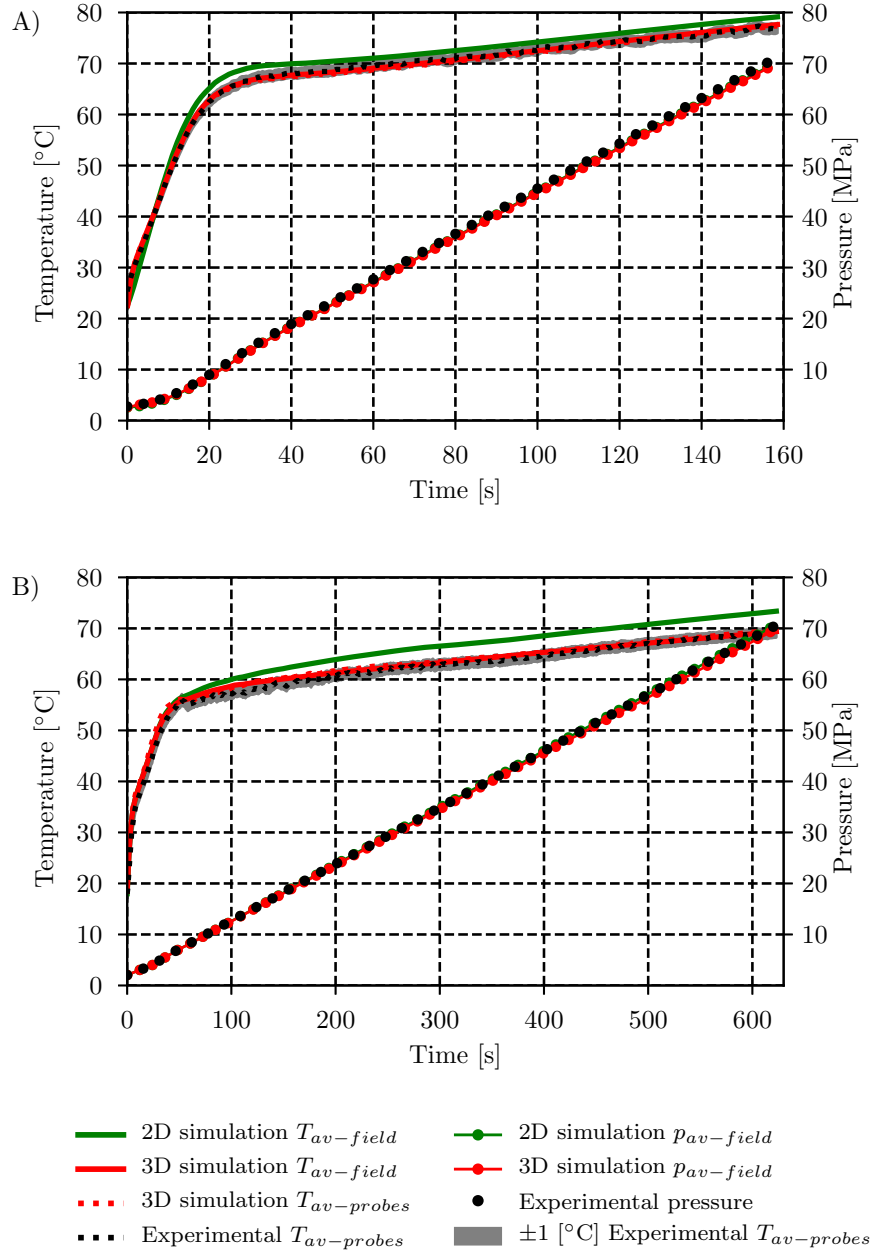


Figure 9: Comparison between the averaged values of the temperature (left axis) and pressure (right axis) issued from the present simulations and the experiment, in the fluid region, for the A) homogeneous and B) heterogeneous cases.

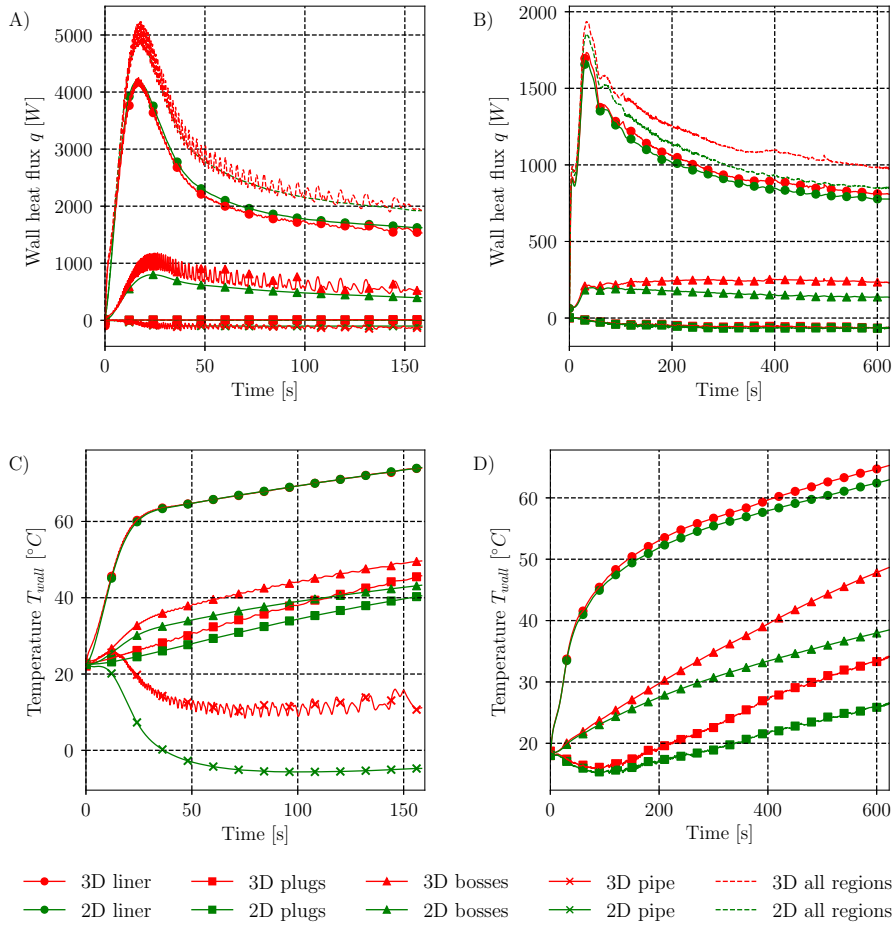


Figure 10: A), B) wall heat flux and C), D) temperature at fluid-solid interfaces as functions of time, for the A), C) homogeneous and B), D) heterogeneous cases.

4.3. Local quantities

330 Figures 11 and 12 present a comparison of probe temperatures issued from the 3D simulations and the experiments, for the homogeneous and the heterogeneous cases, respectively.

In the homogeneous case (figure 11), the simulation globally matches the experimental values. As shown in figure 6 no thermal stratification occurs and the probe values remain close to the averaged temperature value.

335 In the heterogeneous case (12), the simulation results are close to the experimental values until $t = 150$ s, when the thermal gradient starts to develop. Then the simulation tends to underestimate the thermal gradient: in the upper part of the tank (TT760,TT764,TT767), the simulation values are lower than the experimental values and in the lower part of the tank (TT761,TT765,TT768), the simulation values are higher than experimental values. Turbulence is playing a major role in the process of thermal diffusion and its modeling may explain the differences in the heterogeneous case simulation. The $k - \omega$ SST model predicts high levels of turbulent viscosity in regions supposedly laminar. This may result in higher effective thermal diffusion and then in lower gradients of temperature. Homogeneous cases with lower thermal gradients are less impacted by this phenomenon. Turbulence models capturing the laminar-turbulent transition may be a solution. The $k - \omega$ SST Scale-Adaptive Simulation (SAS) [47] has been mentioned by ALAT [46, 35] or the $\Gamma - \Theta$ model [23] has been used by the JRC [21] in the latter study. The emergence of thermal gradients was captured but not their precise magnitudes. The impact of such advanced models remains to be investigated.

5. Conclusion

335 Two filling scenarios of a horizontal gaseous tank, leading to two different thermal behaviors, a homogeneous case and a heterogeneous case, have been simulated and compared to experimental data issued from the HyTransfer project [8]. The simulations have been carried out in 2D using an axisymmetry assumption and in 3D by considering half of the tank.

360 In the homogeneous case, where no thermal stratification occurs, the 2D and 3D simulation averaged temperature are close to the experimental measurements. Due to the restrictions imposed to the fluid under 2D assumption, the inner jet cannot cool areas close to the injector as in the 3D case. This results in a hot spot close to the injector, 10 °C above the averaged temperature at 150 s. A phenomenon of jet flapping is highlighted by the 3D simulations. This phenomenon seems responsible for the periodic motion of the hot spot close to the injector, where the temperature is only 2 °C above the averaged temperature at 150 s. Future work should focus on clarifying jet oscillation mechanism and its link to heat transfer.

370 In the heterogeneous case, where thermal stratification occurs, the 2D simulation does not capture the vertical heterogeneity and the thermal gradient onset cannot be detected. The 3D simulation predicts an averaged temperature

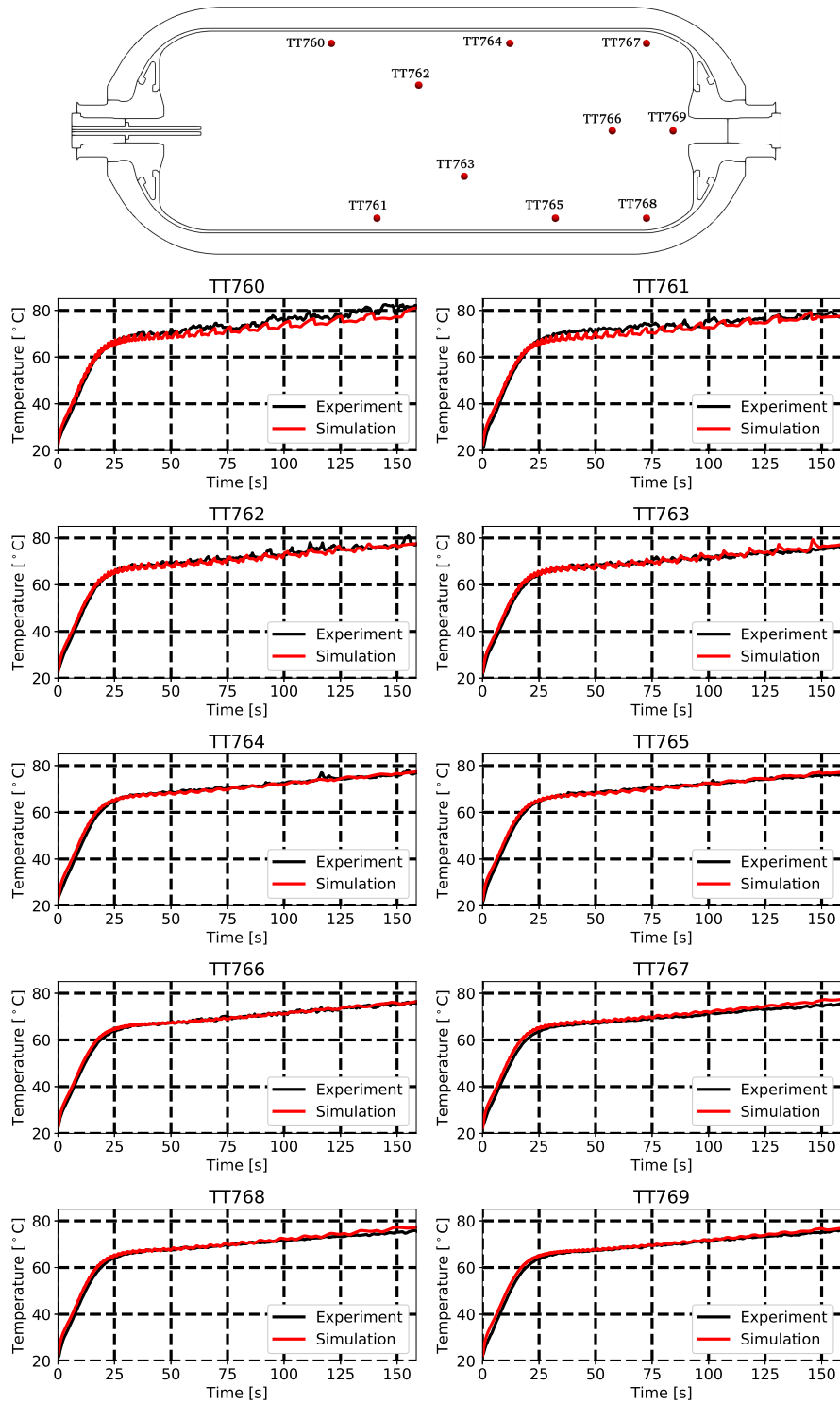


Figure 11: Comparison between the local temperature values issued from the 3D simulation and the experiment, in the homogeneous case. Probe locations are indicated in the upper panel.

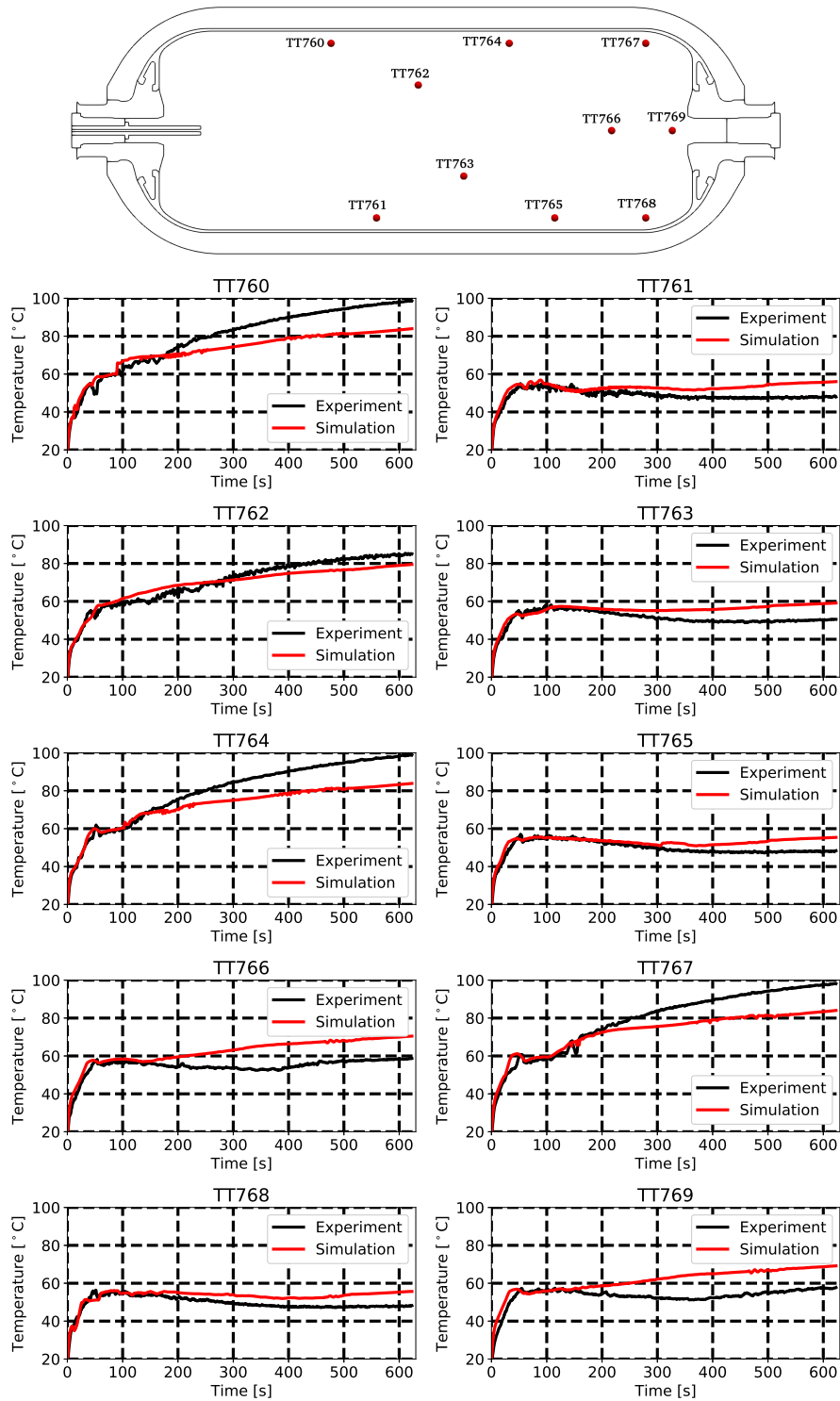


Figure 12: Comparison between the local temperature values issued from the 3D simulation and the experiment, in the heterogeneous case. Probe locations are indicated in the upper panel.

close to the experimental one. It captures the deflection of the jet, which is one of the key processes in the emergence of the thermal gradients. The instant at which the thermal gradients appear is well estimated. The thermal gradients are however underestimated. At the end of the filling process (630 s), the differences of maximum temperature between the simulation results and the experimental measurements at probe TT764 and TT761 are +15 °C and −8 °C, respectively. It is suspected to be a consequence of the $k - \omega$ SST turbulence model which tends to over predict the turbulence level and the associated thermal diffusion. Advanced models like the $k - \omega$ SST SAS model, should be investigated to improve the prediction of thermal gradients.

From a phenomenological perspective, CFD provides insights into the flow physics and thermal behavior inside the tank. Such insights are expected to impact the development of 0D models and help optimizing tank filling strategy.

Acknowledgment

This study was carried on as part of a PhD work funded by Air Liquide Innovation Campus Paris and the National Association of Recherche and Technology (ANRT). It was performed using HPC resources from CALMIP (grants 2019 and 2020, p19025)

References

- [1] Q. Nouvelot, P. Karzel, N. Hart, E. Vyazmina, V. Mattelaer, C. D. Sinding, A. Ruiz, Performance metrics for refuelling protocols for heavy duty hydrogen vehicles, fCH-04-2-2019:Refuelling Protocols for Medium and Heavy-Duty Vehicles (2020).
URL https://prhyde-cdn.s3-accelerate.amazonaws.com/wp-content/uploads/2020/10/14133040/PRHYDE_Deliverable-D2-1_final.pdf
- [2] H. Council, A sustainable pathway for the global energy transition (2017).
URL <http://hydrogencouncil.com/wp-content/uploads/2017/11/Hydrogen-scaling-up-Hydrogen-Council.pdf>
- [3] I. Simonovski, D. Baraldi, D. Melideo, B. Acosta-Iborra, Thermal simulations of a hydrogen storage tank during fast filling, International Journal of Hydrogen Energy 40 (36) (2015) 12560–12571. doi:10.1016/j.ijhydene.2015.06.114.
URL <https://linkinghub.elsevier.com/retrieve/pii/S0360319915015992>
- [4] F. C. S. Committee, Fueling protocols for light duty gaseous hydrogen surface vehicles (dec 2016). doi:https://doi.org/10.4271/J2601_201612.
URL https://doi.org/10.4271/J2601_201612

- 410 [5] D. Melideo, D. Baraldi, CFD analysis of fast filling strategies
for hydrogen tanks and their effects on key-parameters, Inter-
national Journal of Hydrogen Energy 40 (1) (2015) 735–745.
doi:10.1016/j.ijhydene.2014.10.138.
URL [https://linkinghub.elsevier.com/retrieve/pii/
415 S0360319914030146](https://linkinghub.elsevier.com/retrieve/pii/S0360319914030146)
- [6] R. Ortiz Cebolla, B. Acosta, N. de Miguel, P. Moretto, Ef-
fect of precooled inlet gas temperature and mass flow rate on
final state of charge during hydrogen vehicle refueling, Interna-
tional Journal of Hydrogen Energy 40 (13) (2015) 4698–4706.
420 doi:<https://doi.org/10.1016/j.ijhydene.2015.02.035>.
URL [https://www.sciencedirect.com/science/article/pii/
S036031991500364X](https://www.sciencedirect.com/science/article/pii/S036031991500364X)
- [7] Y. Kang, S. M. Cho, D. K. Kim, Charging strategy through
analysis of charging influence factors of ultra-light hydrogen stor-
425 age with polyethylene terephthalate liner, International Jour-
nal of Hydrogen Energy 46 (13) (2021) 9174–9185. doi:<https://doi.org/10.1016/j.ijhydene.2021.01.007>.
URL [https://www.sciencedirect.com/science/article/pii/
S0360319921000148](https://www.sciencedirect.com/science/article/pii/S0360319921000148)
- 430 [8] E. i. European Commission, E. researchers, Hytransfer, FCH JU 2012-1-
325277 (2013).
URL <https://cordis.europa.eu/project/id/325277/reporting>
- [9] W. C. Reynolds, Analytical investigation of the blowdown and charging
processes in a single gas receiver, including the effects of heat transfer,
435 Tech. rep., Stanford University (1955).
- [10] C. Muto, An experimental investigation of the effects of heat transfer during
charging and blowdown of single Gas receivers., 1959.
URL <https://apps.dtic.mil/sti/pdfs/AD0487800.pdf>
- 440 [11] T. Bourgeois, F. Ammouri, M. Weber, C. Knapik, Evaluating the
temperature inside a tank during a filling with highly-pressurized gas,
International Journal of Hydrogen Energy 40 (35) (2015) 11748–11755.
doi:10.1016/j.ijhydene.2015.01.096.
URL [https://linkinghub.elsevier.com/retrieve/pii/
S0360319915001640](https://linkinghub.elsevier.com/retrieve/pii/S0360319915001640)
- 445 [12] V. Molkov, M. Dadashzadeh, D. Makarov, Physical model of on-
board hydrogen storage tank thermal behaviour during fuelling,
International Journal of Hydrogen Energy 44 (8) (2019) 4374–4384.
doi:10.1016/j.ijhydene.2018.12.115.
URL [https://linkinghub.elsevier.com/retrieve/pii/
450 S0360319918340837](https://linkinghub.elsevier.com/retrieve/pii/S0360319918340837)

- [13] T. Terada, H. Yoshimura, Y. Tamura, H. Mitsuishi, S. Watanabe, Thermal behavior in hydrogen storage tank for fev on fast filling (2nd report) (2008). doi:10.4271/2008-01-0463. URL <https://www.sae.org/content/2008-01-0463/>
- 455 [14] C. Devilliers, D7.5 hytransfer final synthesis of the project findings for the industry public (2017).
- [15] O. Redlich, J. N. S. Kwong, On the thermodynamics of solutions. v. an equation of state. fugacities of gaseous solutions., Chemical Reviews 44 (1) (1949) 233–244. doi:10.1021/cr60137a013. URL <https://pubs.acs.org/doi/abs/10.1021/cr60137a013>
- 460 [16] D. Melideo, D. Baraldi, B. Acosta-Iborra, R. Ortiz Cebolla, P. Moretto, CFD simulations of filling and emptying of hydrogen tanks, International Journal of Hydrogen Energy 42 (11) (2017) 7304–7313. doi:10.1016/j.ijhydene.2016.05.262. URL <https://linkinghub.elsevier.com/retrieve/pii/S0360319916307078>
- [17] P. Ouellette, P. G. Hill, Turbulent transient gas injections, Journal of Fluids Engineering 122 (4) (2000) 743–752. doi:10.1115/1.1319845. URL <https://asmedigitalcollection.asme.org/fluidsengineering/article/122/4/743/461883/Turbulent-Transient-Gas-Injections>
- 470 [18] M. C. Galassi, D. Baraldi, B. Acosta Iborra, P. Moretto, CFD analysis of fast filling scenarios for 70 MPa hydrogen type IV tanks, International Journal of Hydrogen Energy 37 (8) (2012) 6886–6892. doi:10.1016/j.ijhydene.2012.01.041. URL <https://linkinghub.elsevier.com/retrieve/pii/S0360319912000912>
- 475 [19] M. C. Galassi, E. Papanikolaou, M. Heitsch, D. Baraldi, B. A. Iborra, P. Moretto, Assessment of CFD models for hydrogen fast filling simulations, International Journal of Hydrogen Energy 39 (11) (2014) 6252–6260. doi:10.1016/j.ijhydene.2013.03.164. URL <https://linkinghub.elsevier.com/retrieve/pii/S0360319913008422>
- 480 [20] D. Melideo, D. Baraldi, M. C. Galassi, R. Ortiz Cebolla, B. Acosta Iborra, P. Moretto, CFD model performance benchmark of fast filling simulations of hydrogen tanks with pre-cooling, International Journal of Hydrogen Energy 39 (9) (2014) 4389–4395. doi:10.1016/j.ijhydene.2013.12.196. URL <https://linkinghub.elsevier.com/retrieve/pii/S0360319913031881>
- 485 [21] D. Melideo, D. Baraldi, N. De Migue, B. Acosta, Effects of the injector direction on the temperature distribution during filling of hydrogen tanks, HySafe, 2017.
- 490

- [22] D. Melideo, D. Baraldi, N. De Miguel Echevarria, B. Acosta Iborra, Effects of some key-parameters on the thermal stratification in hydrogen tanks during the filling process, *International Journal of Hydrogen Energy* 44 (26) (2019) 13569–13582. doi:10.1016/j.ijhydene.2019.03.187.
495 URL <https://linkinghub.elsevier.com/retrieve/pii/S0360319919312169>
- [23] R. B. Langtry, F. R. Menter, Correlation-based transition modeling for unstructured parallelized computational fluid dynamics codes, *AIAA Journal* 47 (12) (2009) 2894–2906. doi:10.2514/1.42362.
500 URL <https://arc.aiaa.org/doi/10.2514/1.42362>
- [24] B. Ravinel, B. Acosta, N. De Migue, P. Moretto, O.-C. Rafael, J. Goran, v. d. L. Ulrich, D4.1 report on the experimental filling test campaign (2017).
505 URL https://s02291b7740b89df1.jimcontent.com/download/version/1493713659/module/11623534399/name/HyTransfer_Report%20on%20the%20experimental%20filling%20test%20campaign_public.pdf
- [25] N. de Miguel, B. Acosta, P. Moretto, R. Ortiz Cebolla, Influence of the gas injector configuration on the temperature evolution during refueling of on-board hydrogen tanks, *International Journal of Hydrogen Energy* 41 (42) (2016) 19447–19454. doi:10.1016/j.ijhydene.2016.07.008.
510 URL <https://linkinghub.elsevier.com/retrieve/pii/S0360319916307340>
- [26] The OpenFOAM foundation (2021).
515 URL <https://openfoam.org/>
- [27] T. Perelman, On conjugated problems of heat transfer, *International Journal of Heat and Mass Transfer* 3 (4) (1961) 293–303. doi:[https://doi.org/10.1016/0017-9310\(61\)90044-8](https://doi.org/10.1016/0017-9310(61)90044-8).
520 URL <https://www.sciencedirect.com/science/article/pii/0017931061900448>
- [28] B. Eckhardt, T. M. Schneider, B. Hof, J. Westerweel, Turbulence transition in pipe flow, *Annual Review of Fluid Mechanics* 39 (1) (2007) 447–468. doi:10.1146/annurev.fluid.39.050905.110308.
525 URL <http://www.annualreviews.org/doi/10.1146/annurev.fluid.39.050905.110308>
- [29] F. R. Menter, Two-equation eddy-viscosity turbulence models for engineering applications, *AIAA Journal* 32 (8) (1994) 1598–1605. doi:10.2514/3.12149.
530 URL <https://arc.aiaa.org/doi/10.2514/3.12149>
- [30] M. Kmecova, O. Sikula, M. Krajcik, Circular free jets: CFD simulations with various turbulence models and their comparison with theoretical

- solutions, IOP Conference Series: Materials Science and Engineering 471 (2019) 062045. doi:10.1088/1757-899X/471/6/062045.
535 URL <http://stacks.iop.org/1757-899X/471/i=6/a=062045?key=crossref.e61902386a0e31c386ae819342bb6b6f>
- [31] A. Meslem, F. Bode, C. Croitoru, I. Nastase, Comparison of turbulence models in simulating jet flow from a cross-shaped orifice, European Journal of Mechanics - B/Fluids 44 (2014) 100–120.
540 doi:10.1016/j.euromechflu.2013.11.006.
URL <https://linkinghub.elsevier.com/retrieve/pii/S0997754613001313>
- [32] A. Aliferis, S. Burkeland, M. Jessen, C. Meek, Pipe flow simulation for reynolds number up to 1 000 000 (2017).
- 545 [33] A. Hedlund, Evaluation of rans turbulence models for the simulation of channel flow, Master’s thesis, Uppsala University, Department of Information Technology.
- [34] L. Fangqing, A thorough description of how WallFunctions are implemented InOpenFOAM, In Proceedings of CFD with OpenSource Software (2016).
550 URL http://www.tfd.chalmers.se/~hani/kurser/OS_CFD_2016
- [35] T. Bourgeois, F. Ammouri, D. Baraldi, P. Moretto, The temperature evolution in compressed gas filling processes: A review, International Journal of Hydrogen Energy 43 (4) (2018) 2268–2292.
555 doi:10.1016/j.ijhydene.2017.11.068.
URL <https://linkinghub.elsevier.com/retrieve/pii/S0360319917343860>
- [36] M. Li, Y. Bai, C. Zhang, Y. Song, S. Jiang, D. Grouset, M. Zhang, Review on the research of hydrogen storage system fast refueling in fuel cell vehicle, International Journal of Hydrogen Energy 44 (21) (2019) 10677–10693. doi:10.1016/j.ijhydene.2019.02.208.
560 URL <https://linkinghub.elsevier.com/retrieve/pii/S0360319919308663>
- [37] E. Lemmon, M. Huber, M. McLinden, Nist standard reference database 23: reference fluid thermodynamic and transport properties-refprop, version 9.1 (2013-05-07 2013).
565 URL https://tsapps.nist.gov/publication/get_pdf.cfm?pub_id=912382
- [38] ChtMultiRegionFoam (2021).
URL <https://openfoamwiki.net/index.php/ChtMultiRegionFoam>
- 570 [39] The PISO algorithm in OpenFOAM (2021).
URL http://openfoamwiki.net/index.php/OpenFOAM_guide/The_PISO_algorithm_in_OpenFOAM

- [40] R. Issa, Solution of the implicitly discretised fluid flow equations by operator-splitting, *Journal of Computational Physics* 62 (1) (1986) 40–65.
575 doi:[https://doi.org/10.1016/0021-9991\(86\)90099-9](https://doi.org/10.1016/0021-9991(86)90099-9).
URL <https://www.sciencedirect.com/science/article/pii/0021999186900999>
- [41] The PIMPLE algorithm in OpenFOAM (2021).
580 URL https://openfoamwiki.net/index.php/OpenFOAM_guide/The_PIMPLE_algorithm_in_OpenFOAM
- [42] L. S. Caretto, A. D. Gosman, S. V. Patankar, D. B. Spalding, Two calculation procedures for steady, three-dimensional flows with recirculation (1973).
- [43] Salome (2021).
585 URL <https://www.salome-platform.org/>
- [44] cfMesh (2021).
URL <https://cfmesh.com/cfmesh/>
- [45] G. Horn, M. W. Thring, Angle of spread of free jets, *Nature* 178 (1956) 205–206. doi:<https://doi.org/10.1038/178205a0>.
- 590 [46] D. Zaepffel, F. Mathey, B. Ravinel, T. Bourgeois, F. Ammouri, CFD analysis of the different flow regimes occurring during the filling of a hydrogen vehicle tank (2016).
- [47] F. Menter, M. Kuntz, R. Bender, A scale-adaptive simulation model for turbulent flow predictions (2003). doi:[10.2514/6.2003-767](https://doi.org/10.2514/6.2003-767).
595 URL <http://arc.aiaa.org/doi/10.2514/6.2003-767>